nature communications

Article

https://doi.org/10.1038/s41467-024-51445-z

Tumor-derived RHOA mutants interact with effectors in the GDP-bound state

Received: 26 July 2023

Accepted: 7 August 2024

Published online: 21 August 2024

Check for updates

Yuan Lin[1] ✉, Theresa A. Ramelot[2], Simge Senyuz[3], Attila Gursoy[4], Hyunbum Jang[5], Ruth Nussinov[5], Ozlem Keskin[6] & Yi Zheng[1] ✉

RHOA mutations are found at diverse residues in various cancer types, implying mutation- and cell-specific mechanisms of tumorigenesis. Here, we focus on the underlying mechanisms of two gain-of-function RHOA mutations, A161P and A161V, identified in adult T-cell leukemia/lymphoma. We find that RHOA^{A161P} and RHOA^{A161V} are both fast-cycling mutants with increased guanine nucleotide dissociation/association rates compared with RHOA^{WT} and show reduced GTP-hydrolysis activity. Crystal structures reveal an altered nucleotide association in RHOA^{A161P} and an open nucleotide pocket in RHOA^{A161V}. Both mutations perturb the dynamic properties of RHOA switch regions and shift the conformational landscape important for RHOA activity, as shown by ^{31}P NMR and molecular dynamics simulations. Interestingly, RHOA^{A161P} and RHOA^{A161V} can interact with effectors in the GDP-bound state. ^{1}H-^{15}N HSQC NMR spectra support the existence of an active population in RHOA^{A161V}-GDP. The distinct interaction mechanisms resulting from the mutations likely favor an RHOA^{WT}-like "ON" conformation, endowing GDP-bound state effector binding activity.

RHOA belongs to the RAS-homology small GTPase family and is a key regulator of a variety of cellular functions[1]. RHOA activity is modulated at several levels, including lipid modification, protein expression, subcellular localization, and association with RHO GDP dissociation inhibitors (RHO GDIs)[2,3]. Importantly, as in most small GTPases, RHOA transduces intracellular signals by acting as a molecular switch that cycles between inactive GDP-bound and active GTP-bound forms[4]. Activation of RHOA involves major conformational changes in two flexible regions, Switch I (residues 28–40) and Switch II (residues 60–78)[4]. This dynamic cycle of GTP-loading/GTP-hydrolysis is essential for proper RHOA signaling and is tightly regulated by guanine nucleotide exchange factors (GEFs) and GTPase-activating proteins (GAPs)[5].

RHOA dysfunction has traditionally been considered to promote cancer proliferation and metastasis[6,7]. Aberrant RHOA signaling in cancer usually stems from RHOA overexpression or hyperactivation via deregulation of its regulators[8]. The role of *RHOA* as a tumor driver gene has recently received increased attention after several human whole cancer genome sequencing studies identified recurrent RHOA mutations in gastric cancer (GC)[9], peripheral T-cell lymphoma (PTCL)[10], adult T-cell leukemia/lymphoma (ATLL)[11], angioimmunoblastic T-cell lymphoma (AITL)[12,13], Burkitt lymphoma (BL)[14], and head and neck squamous cell carcinoma (HNSCC)[15]. Unlike RAS, whose mutations are mostly (98%) found in well-defined hotspots (e.g., G12, G13, and Q61), impair intrinsic and GAP-mediated GTP hydrolysis and/or cause enhanced nucleotide exchange, RHOA mutational hotspots appear highly divergent, vary by tumor type, and display mutation- and tissue-specific biological consequences[16,17]. For example, in solid tumors, RHOA mutations are often located at the effector/regulator binding surface, such as E40Q in HNSCC and R5Q/W, Y42C, and L57V in

[1]Experimental Hematology and Cancer Biology, Cincinnati Children's Hospital Medical Center, Cincinnati, OH, USA. [2]Center for Biotechnology and Interdisciplinary Studies, Rensselaer Polytechnic Institute, Troy, NY, USA. [3]Computational Sciences and Engineering, Koc University, Rumelifeneri Yolu, Istanbul, Turkey. [4]Department of Computer Engineering, Koc Univeristy, Rumelifeneri Yolu, Istanbul, Turkey. [5]Computational Structural Biology Section, Frederick National Laboratory for Cancer Research in the Cancer Innovation Laboratory, National Cancer Institute, Frederick, MD, USA. [6]Department of Chemical and Biological Engineering, Koc Univeristy, Rumelifeneri Yolu, Istanbul, Turkey. ✉e-mail: yuan.lin@cchmc.org; yi.zheng@cchmc.org

GC[9]. In T-cell leukemia, RHOA mutations are almost always located in the nucleotide-binding pocket. In ATLL, in addition to the most prevalent hotspot, G17V, shared with PTCL and AITL, other previously undescribed RHOA mutations have been identified, including C16R/F, A161P/V, and K118E/Q[11]. Some RHOA mutations seem to be gain-of-function mutations (e.g., C16R/F, A161P/V, and K118E/Q), whereas others may be loss-of-function or even behave as dominant-negative mutations (e.g., G17V and A161E).

To understand the unique role of distinct RHOA mutations in different tumor types and their seemingly different functions[18–20], it is critical to better characterize RHOA mutants, particularly the structural features that lead to their unique behavior. We have focused on two putative gain-of-function RHOA mutations identified in ATLL, A161P and A161V, to study their impact on both structure and function using a combination of biochemical analyses, crystallography, NMR spectroscopy, and molecular dynamics (MD) simulations. Residue A161 is located in the SAK motif, one of the conserved G-motifs across the small GTPase superfamily for guanine nucleotide binding and GTPase activity. Although mutations at A161 in RHOA are not as frequent (i.e. 11 cases of A161V and two cases of A161P documented in the COSMIC database[21]), mutations at the equivalent position have been found in KRAS (342 cases of A146T, 98 cases of A146V, and 29 cases of A146P), HRAS (two cases of A146T and two cases of A146V), NRAS (24 cases of A146T, four cases of A161V, and one case of A146P), and RAC1 (22 cases of A159V) in the same database. It is therefore important to understand how these mutations confer oncogenicity at the molecular and atomic level. Here, we reported that in RHOA, the A161V and A161P mutations contribute to faster nucleotide exchange via a unique mechanism. We further establish that $RHOA^{A161P}$ and $RHOA^{A161V}$ can bind to effectors even in a GDP-bound state, suggesting that these mutations cause conformational changes that enforce and stabilize an active conformation in the absence of bound GTP.

Results

$RHOA^{A161V}$ and $RHOA^{A161P}$ are fast-cycling mutants with reduced GTPase activity

Throughout this study, RHOA constructs were truncated at residue 181 (ΔC) and contained the F25N mutation, known to stabilize protein expression in bacteria[22]. C-terminal truncation has little impact on RHOA's biochemical properties, whereas F25N reduces interaction with the effector (Supplementary Fig. 1). For simplicity, we termed this modified construct $RHOA^{WT}$. Two lab-generated mutations, F30L and T37A, were included as controls for biochemical analyses. $RHOA^{F30L}$ is a known fast-cycling mutant[23] and $RHOA^{T37A}$, equivalent to $HRAS^{T35A}$, is a constitutively inactive mutant with impaired interaction with effectors[24]. Slow hydrolyzable GTP analogs such as GMPPNP or GTPγS were used, and no significant difference was detected between these analogs (Supplementary Fig. 2).

Mutations at residue A161 are expected to affect nucleotide-binding kinetics. Indeed, $RHOA^{A161P}$ and $RHOA^{A161V}$ had significantly increased nucleotide dissociation rates (k_{off}) compared with $RHOA^{WT}$ under both Mg^{2+} (Fig. 1a, b) and EDTA conditions (Supplementary Fig. 3a). Mg^{2+} is an essential cofactor for small GTPases and removing Mg^{2+} with EDTA greatly reduces affinity for nucleotides[25]. $RHOA^{A161P}$ and $RHOA^{A161V}$ also showed significantly increased nucleotide association rates (k_{on}) compared with $RHOA^{WT}$ (Supplementary Fig. 3b). Increased k_{on} and k_{off} are likely coupled events. $RHOA^{A161V}$ had a slightly higher k_{on}, but no change in k_{off} than $RHOA^{A161P}$ (Fig. 1b and Supplementary Fig. 3b). $RHOA^{A161P}$ and $RHOA^{A161V}$ had ~9-10-fold higher k_{off} and ~2-3-fold higher k_{on} than $RHOA^{F30L}$, indicating a more profound perturbation of the nucleotide pocket by A161P/V than by F30L. T37A, on the other hand, reduced k_{on} and k_{off} to ~50% (Supplementary Fig. 3a, b, Supplementary Table 1). MBP-tagged functional DH/PH domains of LARG, an RHOGEF, showed increased binding to $RHOA^{A161P}$ and $RHOA^{A161V}$ preloaded with GDP or GMPPNP, in contrast to $RHOA^{WT}$ which only bound to the GEF when EDTA was added to chelate Mg^{2+} and release nucleotides (Fig. 1c). Both mutants showed reduced binding to LARG when extra nucleotides were supplemented, distinguishing them from dominant negative mutants. In contrast, $RHOA^{F30L}$ displayed a minimal increase in binding to LARG in GDP/GMPPNP-bound forms and $RHOA^{T37A}$ had much reduced complex formation even in the EDTA condition (Supplementary Fig. 3d). The two mutants, particularly $RHOA^{A161P}$, had complex formation with LARG in the GDP- and GMPPNP-states (Fig. 1c) and less nucleotide loading (Supplementary Fig. 3b), indicating impaired binding to nucleotides.

To measure GTPase activity, we used an assay that relies on the enzymatic conversion of GTP that remains after the GTPase reaction to ATP and the detection of the generated ATP using a luciferin/luciferase combination[26]. Excess GTP substrate was used and GTP hydrolysis occurred after GDP/GTP exchange, distinct from other single-turnover GTPase assays. 20 mM EDTA was present in the reaction buffer to minimize the effects of the difference in nucleotide exchange rates on evaluating their GTPase ability. $RHOA^{A161P}$ and $RHOA^{A161V}$ displayed ~2-fold reduced intrinsic and ~3-fold reduced p190, a RHOGAP, stimulated GTPase activity compared to $RHOA^{WT}$ (Fig. 1d, e, Supplementary Fig. 3c, and Supplementary Table 2). The hydrolysis impairment could be underestimated as both mutants cycle GDP/GTP faster even in the EDTA condition (Supplementary Fig. 3a). $RHOA^{F30L}$ showed little change. $RHOA^{T37A}$ showed a much reduced intrinsic and GAP-stimulated GTPase activity, consistent with the previous result in RAS[27]. Thus, $RHOA^{A161P}$ and $RHOA^{A161V}$ are fast-cycling GTPases with increased dissociation and association rates, destabilized nucleotide binding, and reduced GTP hydrolysis activity.

GTP-bound $RHOA^{A161V}$ exhibits significant perturbation and increased state 1, whereas $RHOA^{A161P}$ is similar to $RHOA^{WT}$ in ^{31}P NMR spectra

^{31}P NMR spectroscopy has been used to probe the conformations around bound nucleotides in small GTPases[28]. When examining the slow hydrolyzable GTP analog GTPγS-bound protein, we previously revealed that RHOA exists in at least two conformational states[29]. To explore possible perturbations in the nucleotide-binding environment of the A161P and A161V RHOA mutants, we collected ^{31}P NMR spectra of GDP-, GMPPNP-, and GTPγS-bound $RHOA^{A161P}$ and $RHOA^{A161V}$, as well as $RHOA^{WT}$, $RHOA^{F30L}$, and $RHOA^{T37A}$ at 275 K and 298 K. We focused on examining the changes in both the chemical shift values and the shifts in the equilibrium between the conformational states.

When bound to GDP, all three mutants showed relatively unperturbed chemical shifts of β-phosphate, whereas α-phosphate showed a downfield shift (Fig. 2a, Supplementary Fig. 4a, and Supplementary Table 3). Interestingly, we observed a resonance close to the free nucleotide at the α-phosphate in $RHOA^{F30L}$-GDP and $RHOA^{A161V}$-GDP, suggesting a state with an open binding-site conformation near the α-phosphate. This resonance was unlikely from free GDP as there was no (or very little) β_{GDP} resonance. In contrast, free GDP in the same buffer showed comparable resonances at both phosphates. We arbitrarily designated the downfield peak as state 1 and the other as state 2. In $RHOA^{A161P}$-GDP, state 1 was negligible and its spectrum was similar to $RHOA^{WT}$-GDP. The A161P and A161V mutations also influenced the ^{31}P resonances of RHOA in complexes with GMPPNP (Fig. 2b, Supplementary Fig. 4b, and Supplementary Table 3). $RHOA^{A161P}$ exhibited only minor chemical shift changes, whereas $RHOA^{A161V}$ and $RHOA^{F30L}$ were significantly different for all three ^{31}P shifts.

In contrast to the GDP- and GMPPNP-bound RHOA proteins, we observed only minor chemical shift changes in the GTPγS-bound mutant proteins (Fig. 2c, Supplementary Fig. 4c, and Supplementary Table 4). Rather, we identified shifts in the conformational equilibrium, with $RHOA^{A161V}$ and $RHOA^{F30L}$ being the most striking. The ^{31}P peaks corresponding to different conformational states coalesced into a single peak at increasing temperatures, indicating that they underwent

rapid exchange (Supplementary Fig. 5). When bound to GTPγS, RHOA^{A161P} displayed a pattern similar to RHOA^{WT} (Supplementary Table 4). State 2 is the active state with stronger effector affinity (Fig. 2d), consistent with previously published RHOA^{WT} titration data[29]. RHOA^{A161V}, on the other hand, displayed a different pattern. The resonance peak of α-phosphate was broadened and likely dominated by state 1, and titration of GST-RHOTEKIN-RBD resulted in a partial shift to state 2 (Fig. 2e). The resonance peak of β-phosphate indicates two or more possible states, with the dominant state most likely inactive and designated as state 1, and the downfield peak possibly active and designated as state 2 (Fig. 2e). Strikingly, we observed three peaks in the γ-phosphate resonance, with the dominant state designated as state 1′ in RHOA^{T37A} and two other peaks as state 1 and state 2 in RHOA^{WT}. The observation of both state 1′ and state 1 supports the hypothesis that the state 1 conformation in RHOA^{WT} differs from RHOA^{T37A}, which could be similar to the inactive HRAS state 1 conformation represented by RAS^{T35S}. RHOA^{F30L} showed a pattern similar to that of RHOA^{A161V} (Fig. 2f) and both have more heterogeneous states than RHOA^{WT} and RHOA^{A161P} (Fig. 2c).

RHOA^{A161V} exhibits an enlarged nucleotide-binding pocket, whereas RHOA^{A161P} displays altered nucleotide interaction in crystal structures

To better interpret our biochemical analyses, we solved the crystal structures of RHOA^{A161P} and RHOA^{A161V} in complex with GDP at 1.5 Å and 1.4 Å resolutions, respectively (Fig. 3a and Supplementary Table 5). Complexed ligands were confirmed with omit maps (Supplementary Fig. 6). We previously determined the crystal structures of RHOA^{WT} in complex with GDP or GMPPNP (PDB IDs 6V6U and 6V6M)[29]. Similar to RHOA^{WT}-GDP and RHOA^{WT}-GMPPNP, GDP-bound RHOA^{A161P} and RHOA^{A161V} were packed in the space group $P2_1$, featuring the characteristic P36-Mg^{2+} coordination (Supplementary Fig. 7a) instead of the

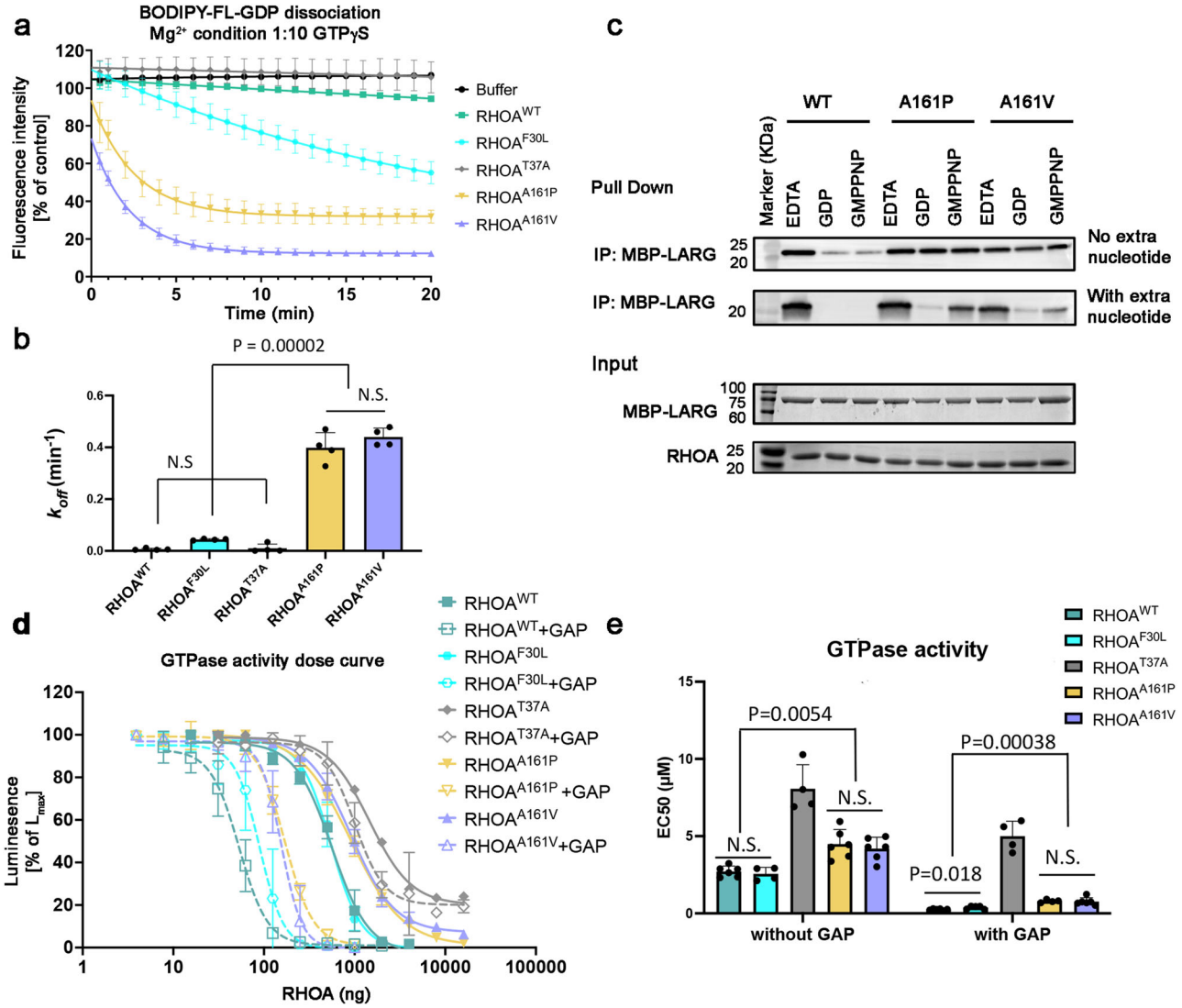


Fig. 1 | Analysis of wild-type and mutant RHOA biochemical properties. **a** Nucleotide dissociation assays for RHOA^{WT} (teal), RHOA^{F30L} (cyan), RHOA^{A161P} (orange), RHOA^{A161V} (purple) with RHOA-BODIPY-FL-GDP: GTPγS ratio of 1:10 in the presence of Mg^{2+}. Data represents mean ± SD with $n = 4$ biological repeats. **b** Statistical analysis (unpaired t-test) of dissociation rates obtained from fitting data in **a**. Data represents mean ± SD. **c** Pull-down assays with MBP-LARG-DH/PH to detect binding of purified wild-type and mutant RHOA proteins preloaded with GDP or GMPPNP or in the presence of EDTA. The pull-down has been done with or without supplemented nucleotides. The pull-down has been repeated three times with similar results. **d** Measurement of RHOA intrinsic or GST-p190-GAP stimulated GTPase activity. GTPase activity of wild-type and mutant RHOA at different concentrations was measured with or without 2 μM GST-P190-GAP. Data represents mean ± SD with $n = 4$–6 biological repeats. **e** Statistical analysis (unpaired t-test) of EC50s from fitting data in **d**. Data represents mean ± SD. RHOA^{T37A} is significantly different from the others and the P value is not shown ($P < 0.00001$). Source data are provided as a Source Data file.

https://doi.org/10.1038/s41467-024-51445-z

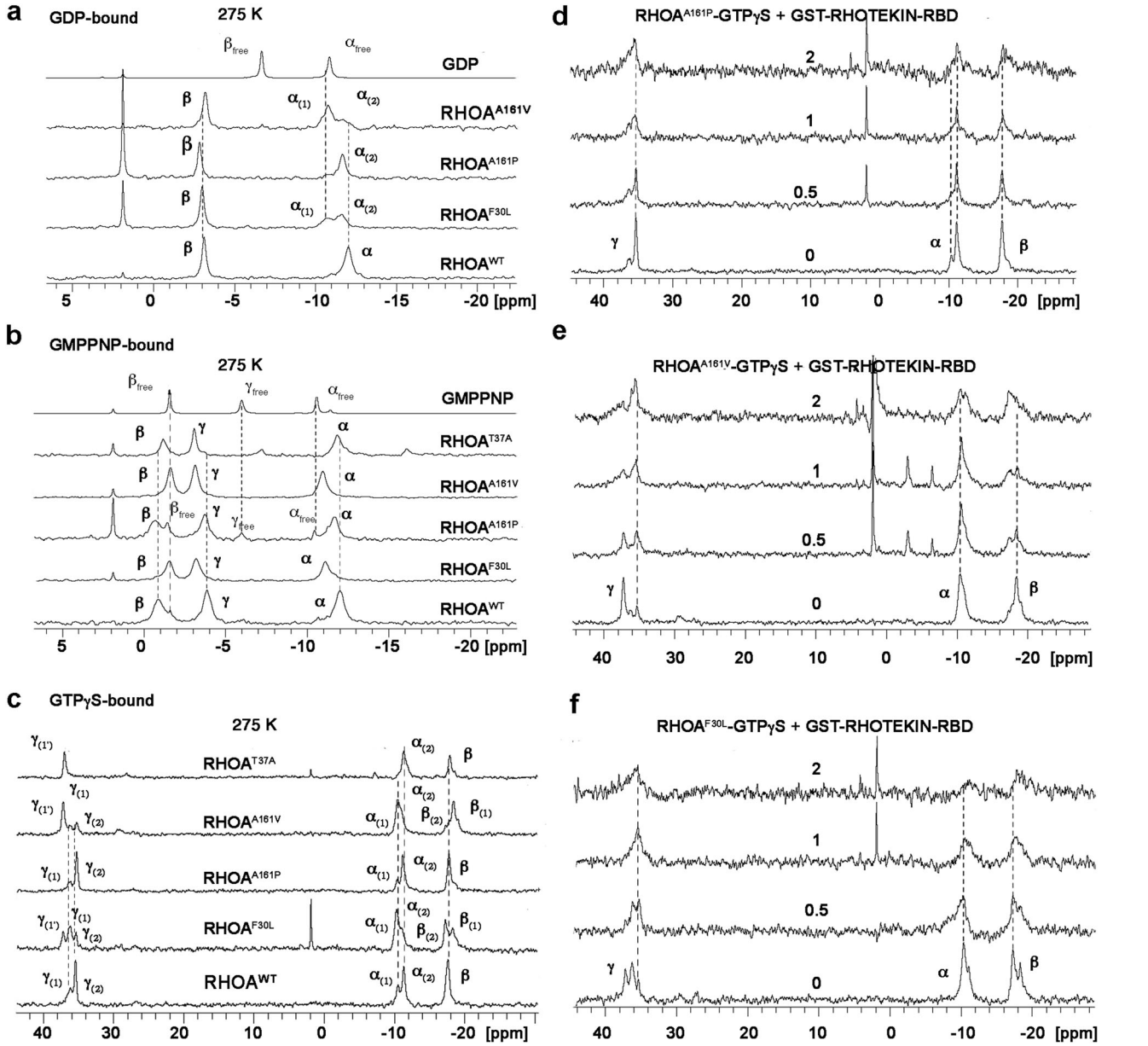


Fig. 2 | ^{31}P NMR spectra of GDP-, GMPPNP-, and GTPγS-bound RHOA^{WT} and mutants. a Comparison of ^{31}P NMR spectra of GDP-bound RHOA^{WT} (0.84 mM), RHOA^{F30L} (0.71 mM), RHOA^{A161P} (0.40 mM), and RHOA^{A161V} (0.63 mM) at 275 K. Both RHOA^{A161V} and RHOA^{F30L} showed an additional state at the α-phosphate that possibly has an open conformation around the α-phosphate. This state was barely detectable in RHOA^{A161P}. **b** Comparison of ^{31}P NMR spectra of GMPPNP-bound RHOA^{WT} (0.67 mM), RHOA^{F30L} (0.62 mM), RHOA^{A161P} (0.45 mM), RHOA^{A161V} (0.44 mM), RHOA^{T37A} (0.51 mM) at 275 K. **c** Comparison of ^{31}P NMR spectra of GTPγS-bound RHOA^{WT} (0.60 mM), RHOA^{F30L} (0.63 mM), RHOA^{A161P} (0.56 mM), RHOA^{A161V} (0.67 mM), and RHOA^{T37A} (0.7 mM) at 275 K. At the γ-phosphate, RHOA^{A161P} was very similar to RHOA^{WT}. In contrast, RHOA^{A161V} and RHOA^{F30L} displayed two inactive states, state 1 as in RHOA^{WT} and state 1′ as in RHOA^{T37A}. To better understand the nature of the states, ^{31}P NMR spectra of RHOA^{A161P} (**d**), RHOA^{A161V} (**e**), and RHOA^{F30L} (**f**) in complex with GST-RHOTEKIN-RBD were collected at 275 K. RHOA^{WT} titrations with GST-RHOTEKIN-RBD and GST control have been published previously[29]. The molar ratio of GST-RHOTEKIN-RBD/RHOA increases from 0, 0.5, 1, to 2, starting from ~0.5 mM RHOA proteins. All spectra were aligned with the inorganic phosphate Pi peak.

always observed T37 (T35 in RAS) in most small GTPase structures. Compared with RHOA^{WT}-GDP, there was only minimal conformational variation for RHOA^{A161P}-GDP and RHOA^{A161V}-GDP. They all adopted a more "open" conformation for the N-terminal part of Switch I, with the nucleotide and P-loop highly exposed to the solvent. Unsurprisingly, two key residues, Y34 and Q63, adopted positions and interactions similar to those in the previous RHOA^{WT}-GDP structure (Supplementary Fig. 7b, c).

Compared with RHOA^{WT}-GDP, the A161V mutant displayed no change in nucleotide interactions based on the crystal structure. Two dioxane molecules from the crystallization solutions were identified to stabilize the guanine base and ribose in RHOA^{A161V}-GDP (Supplementary Fig. 7e). RHOA^{A161P}, however, displayed clear alterations in nucleotide interactions around the guanine group. In RHOA^{WT}-GDP, RHOA^{WT}-GMPPNP, and RHOA^{A161V}-GDP, two conserved water molecules coordinated a hydrogen-bond network between the guanine base and the main chain of G17 and K118, and the side chain of N117 (Fig. 3b). In RHOA^{A161P}, both water molecules were absent (Fig. 3c); instead, proline formed stacking interactions with the base. In addition, the dioxane molecule perpendicular to the guanine base in RHOA^{WT}-GDP and RHOA^{A161V}-GDP was missing in RHOA^{A161P}-GDP (Supplementary Fig. 7f). Loop L10, where A161 resides, shows ~0.4–0.7 Å displacement in

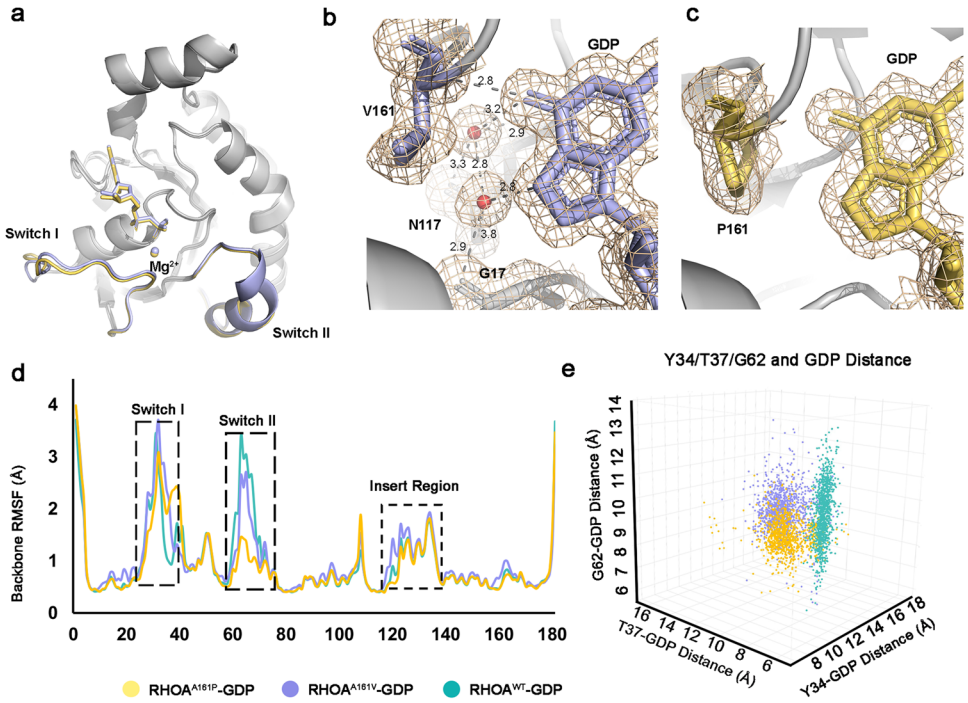


Fig. 3 | Structural analysis and MD simulation of RHOA^{A161P}-GDP and RHOA^{A161V}-GDP. a Overall fold of GDP-bound RHOA^{A161P} and RHOA^{A161V}. The switch regions are colored orange (RHOA^{A161P}) or purple (RHOA^{A161V}), encompassing residues 28–40 and 60–78, respectively. **b** Two conserved water molecules mediate a hydrogen-bond network between the nucleotide guanine base and RHOA, as exemplified in RHOA^{A161V}-GDP. Electron densities around the GDP, the two water molecules, residue 161, and other surrounding residues are contoured at 1σ (wheat) from the 2Fo-Fc map. **c** These two water molecules are missing in RHOA^{A161P}-GDP. **d** Backbone RMSF plot for RHOA-GDP systems. **e** The distances of important residues and GDP. Y34, T37, and G62 distances were calculated using C_α of the residues and β-phosphate. Source data are provided as a Source Data file.

RHOA^{A161V} and RHOA^{A161P} in opposite directions (Supplementary Fig. 7d). The solvent-accessible area of the nucleotide was increased in RHOA^{A161V}-GDP (1273.2 Å^2) and decreased in RHOA^{A161P}-GDP (1188.8 Å^2), compared with RHOA^{WT}-GDP (1249.1 Å^2), suggesting RHOA^{A161V}-GDP has a more open nucleotide-binding pocket.

Although RHOA^{A161V} showed major changes around the phosphates in ^{31}P NMR spectra, we did not observe significant changes in its crystal structure. This is unsurprising as both switch regions participate in crystal contacts in most RHOA apo crystal structures. Crystallization conditions favor a selected conformational state from multiple possible ones that RHOA could adopt in solution. Exploring alternative crystallization conditions may help reveal additional conformational states. Another key feature we examined was the internal mobility of the switch regions. Due to the limitation of crystal structures, this information is only weakly predictive of motions in solution. Both RHOA^{A161P}-GDP and RHOA^{A161V}-GDP crystal structures showed improved electron densities around the Switch I region compared with RHOA^{WT}-GDP (Supplementary Fig. 7e, f), and the modified B-factor plot indicated slightly decreased flexibility in the N-terminus of Switch I (Supplementary Fig. 7g). The Switch II loop shows no change, and the effects of the mutants may have been masked by crystallographic contact.

RHOA^{A161V} displays a more open Switch I, whereas RHOA^{A161P} shows a closed Switch II in molecular dynamics (MD) simulations

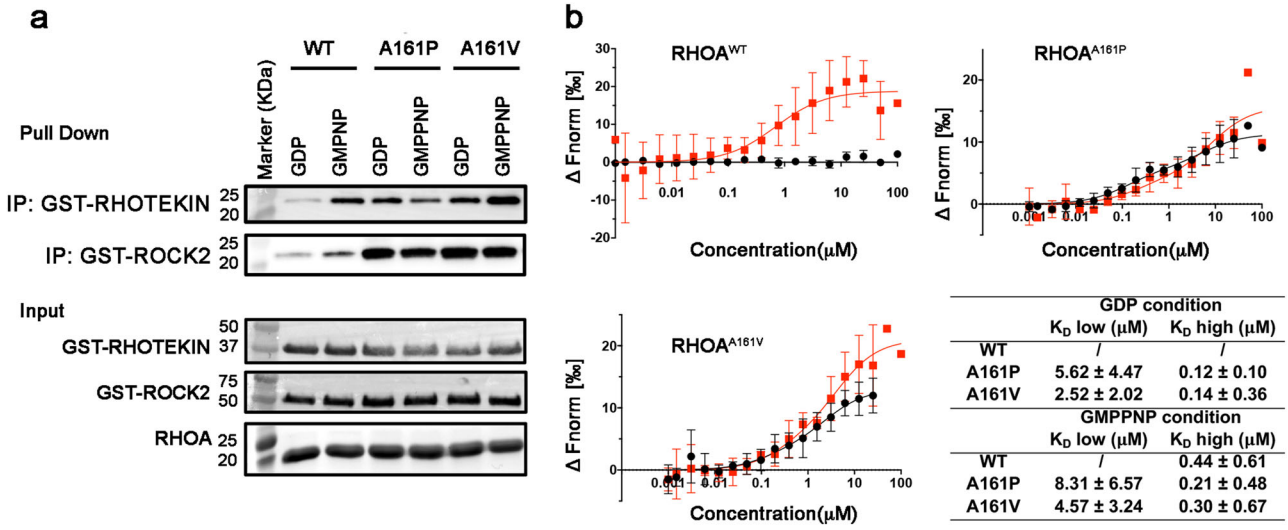
To complement the crystallographic and NMR analyses, the molecular dynamics (MD) trajectories of GDP-bound RHOA^{WT}, RHOA^{A161P}, and RHOA^{A161V} systems were analyzed. 1 µs MD simulation of each system was performed, and all systems were stable during the simulation (Supplementary Fig. 8a). Several analyses, including root-mean-square fluctuations (RMSF), clustering of trajectories, and distances between selected switch residues and GDP, were performed throughout the simulation trajectories.

Higher RMSF are associated with larger structural fluctuations. According to the backbone RMSF, Switch I showed similar fluctuations for all systems except around E40, which showed higher fluctuations in RHOA^{A161P} (Fig. 3d). In the Switch II region, RHOA^{A161P} exhibited comparably smaller fluctuations, suggesting a possible transition to active-like state 2 in RHOA^{A161P} that was less prominent in RHOA^{A161V}. We also observed large fluctuations in the insert region for all systems, which is involved in activation and effector binding.

To characterize Switch I/II conformations, we calculated the distances between Y34/T37/G62 and GDP (Supplementary Table 6). From the distance distributions of Y34-to-GDP and T37-to-GDP, it can be seen that the mutated systems had more diverse Switch I conformations (Fig. 3e). They had a higher standard deviation of the Y34/T37 to GDP distances, which supports the conformational diversity of Switch I (Supplementary Table 6). Comparing the standard deviations of the distances, Switch I of RHOA^{A161P} was more diverse than RHOA^{A161V}. RHOA^{A161P} had varying Switch I distances, which may indicate a transition between states 1 and 2, whereas RHOA^{A161V} appeared to be in state 1 (Fig. 3e and Supplementary Fig. 8b). In contrast to the Switch I conformation, the Switch II conformation of RHOA^{WT} was more diverse, with a large standard deviation in the G62-to-GDP distance (Supplementary Table 6). Switch II of RHOA^{A161P} has a more closed conformation than that of RHOA^{WT}. The RHOA^{WT}, RHOA^{A161P}, and RHOA^{A161V} trajectories were clustered, and the three most populated clusters were analyzed further (Supplementary Table 7). The most populated cluster of RHOA^{A161P} had a more closed Switch I, whereas Switch I of RHOA^{A161V} was more open (Supplementary Fig. 8c), consistent with the crystallographic data.

With a combination of biochemical analyses, ^{31}P NMR spectroscopy, crystallography, and MD simulations, we demonstrated that mutations A161P and A161V have different atomic mechanisms underlying their fast-cycling behavior. A161P alters the interaction with the nucleotide, reduces the fluctuation of Switch II, and barely shifts

https://doi.org/10.1038/s41467-024-51445-z



	GDP condition	
	K_D low (μM)	K_D high (μM)
WT	/	/
A161P	5.62 ± 4.47	0.12 ± 0.10
A161V	2.52 ± 2.02	0.14 ± 0.36
	GMPPNP condition	
	K_D low (μM)	K_D high (μM)
WT	/	0.44 ± 0.61
A161P	8.31 ± 6.57	0.21 ± 0.48
A161V	4.57 ± 3.24	0.30 ± 0.67

Fig. 4 | GDP-bound mutant RHOA^{A161V} and RHOA^{A161P} interact with effectors. **a** Pull-down assay with GST-RHOTEKIN-RBD and GST-ROCK2-RBD to detect the binding of purified wild-type and mutant RHOA proteins preloaded with GDP or GMPPNP. The pull-down has been repeated five times with similar results. **b** Microscale thermophoresis analysis of the direct binding between GDP- (black) or GMPPNP-bound (red) RHOA proteins and RHOTEKIN-RBD. ΔFnorm [‰] = 10*(Fnorm(bound) − Fnorm(unbound)). Data represents mean ± SD with $n = 8$ biological repeats for RHOA^{WT}-GMPPNP and $n = 3$ for all other samples. K_D values obtained from the binding curves are listed and shown in μM. Source data are provided as a Source Data file.

the conformation equilibrium when GTP-bound. On the other hand, A161V greatly impacts the conformations around the active site, opens the Switch I loop, and shifts the conformation towards the inactive states when bound to GTP.

RHOA^{A161P} and RHOA^{A161V} bind to effectors in the GDP-bound state

To evaluate the effects of RHOA mutations on signaling, we tested the binding activity of RHOA^{A161P}, RHOA^{A161V}, and RHOA^{WT} to two known effectors that contain two different types of RHO binding domain (RBD): RHOTEKIN and ROCK2. We used the canonical in vitro RHOA activity assay with the RBD of RHOTEKIN or ROCK2 tagged to GST and immobilized to beads. Intriguingly, while RHOA^{WT} showed complex formation with RHOTEKIN-RBD or ROCK2-RBD only in the presence of GMPPNP, RHOA^{A161V} and RHOA^{A161P} showed complex formation under both GDP and GMPPNP conditions. The binding of GDP-bound mutants was unlikely to be non-specific, as GST and GST-PAK1-RBD didn't pull down the complex (Supplementary Fig. 9a, b). RHOA proteins without the F25N mutation showed a similar pattern (Supplementary Fig. 9c). In contrast, the equivalent mutation A159V in RAC1 resulted in little binding to PAK1-RBD in the GDP state (Supplementary Fig. 9d, e), indicating that the functional consequence of a particular mutation is GTPase-specific.

The relative amount of complex forming with effectors between the mutants' GDP- and GTP-bound states was inconsistent in pull-down assays, likely due to structural heterogenicity and impaired nucleotide binding to different extents of RHOA mutants. To quantify, we measured the direct interaction between RHOA and RHOTEKIN-RBD using microscale thermophoresis (MST). While RHOA^{WT}-GDP showed no binding to RHOTEKIN-RBD, as expected, RHOA^{A161V} and RHOA^{A161P} bound RHOTEKIN-RBD even in the GDP-bound state (Fig. 4b). Although the binding curves of both nucleotide states of RHOA^{A161P} and RHOA^{A161V} were fitted the best with a two-state binding model, we do not have evidence that this resulted from two populations. The high K_D of both mutants was similar to that of RHOA^{WT}-GMPPNP, indicating that the mutations have no significant effect on effector affinity.

To further confirm the binding interaction, we titrated GST-RHOTEKIN-RBD to RHOA^{A161V}-GDP and collected ^{31}P NMR spectra. Titration resulted in slight chemical shift changes at both phosphates in RHOA^{A161V}-GDP (Supplementary Fig. 10a), supporting the pull-down and MST results. The chemical shift changes were not observed in RHOA^{WT}-GDP titrated with GST-RHOTEKIN-RBD or RHOA^{A161V}-GDP titrated with GST (Supplementary Fig. 10b). However, titration of the effector did not clearly change the ratio of the states in RHOA^{A161V}-GDP; thus, we could not assign a particular state as active or inactive.

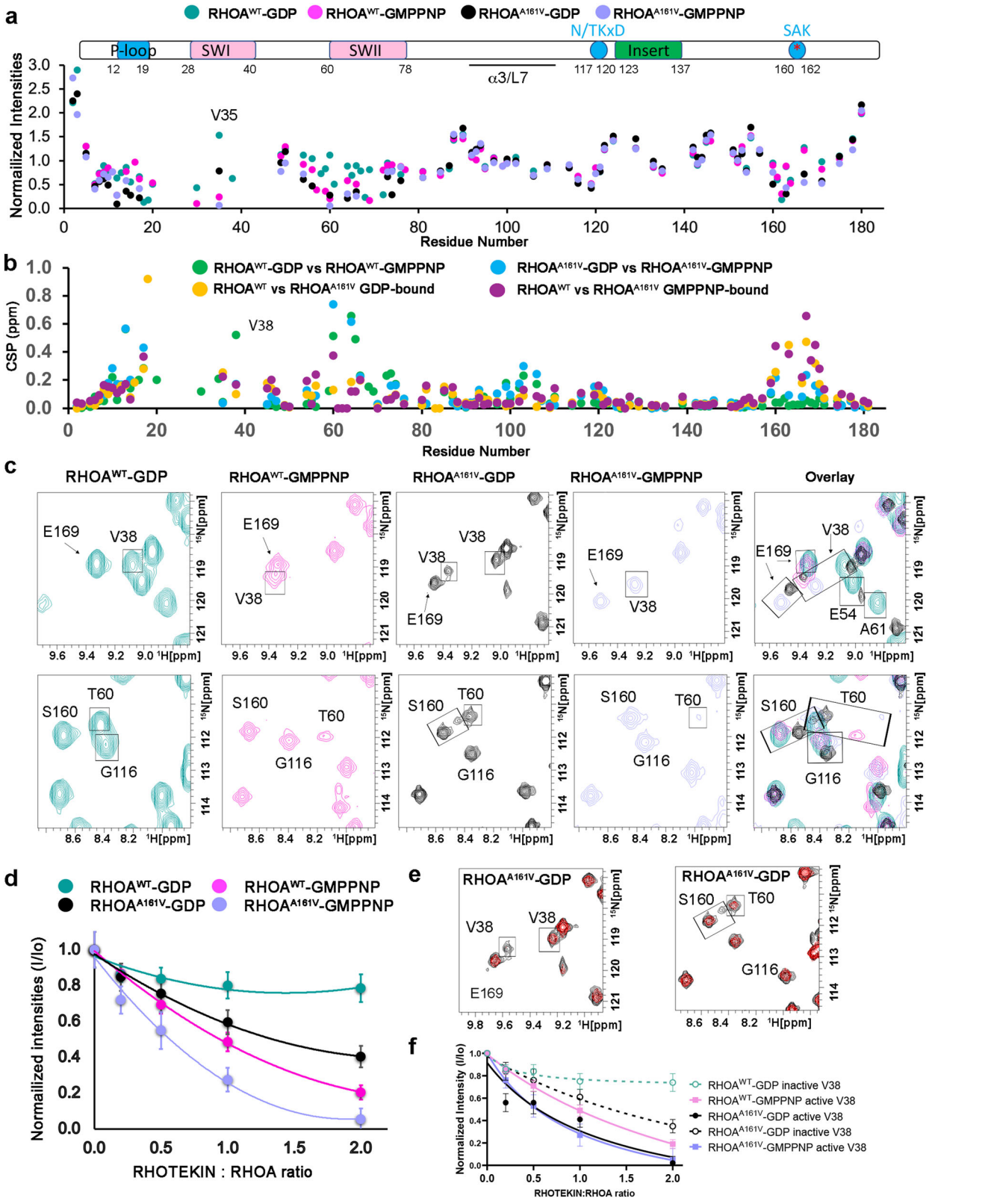
RHOA^{A161V}-GDP contains a population with "ON"-like conformation in ^{1}H-^{15}N HSQC NMR

To examine the overall conformational changes caused by the A161V mutation, we collected ^{1}H-^{15}N HSQC spectra for ^{15}N-labeled RHOA^{WT} and RHOA^{A161V} in both GDP- and GMPPNP-bound forms (Supplementary Fig. 11a) and seek evidence of an "ON" conformation in RHOA^{A161V}-GDP. RHOA^{A161P} was not included due to its impaired binding to GMPPNP (Fig. 1c) and low protein yield. Based on previous assignments for RHOA$^{\Delta C}$-GDP (BMRB ID 16668), RHOA$^{\Delta C}$-GTPγS (BMRB ID 16669), and ^{1}H-^{15}N nuclear Overhauser effect spectroscopy (NOESY) spectra, we were able to transfer most of the non-overlapping amide peak assignments to the ^{1}H-^{15}N HSQC spectra (Supplementary Figs. 12–15).

There were some changes in the spectrum of our RHOA^{WT}-GDP protein (ΔC, F25N) compared with the published result of RHOA$^{\Delta C}$-GDP (BMRB ID 16668)[30], likely caused by the F25N mutation. For example, K18 and T19 in the P-loop and R68, L69, and R70 in Switch II were assigned in RHOA^{WT}-GDP (ΔC, F25N), but not in RHOA$^{\Delta C}$-GDP. In RHOA$^{\Delta C}$-GTPγS (BMRB ID 16669), a significant number of peak assignments were missing in the P-loop, SAK motif, and switch regions. In RHOA^{WT}-GMPPNP (ΔC, F25N), we were able to assign more peaks in these regions, including G12, D13, A15, C20, F30, Y34, V35, V38, D59, T60, E64, Y66, R68, R70, A161, and K162. This agrees with our previous finding that GMPPNP-bound RHOA had faster exchange rates between states than GTPγS-bound RHOA[29], which resulted in sharper peaks. Therefore, we collected the spectra of RHOA proteins in complex with GMPPNP at 298 K to maximize detectable peaks in the flexible regions.

When comparing the ^{1}H-^{15}N HSQC spectra of all four samples, the first obvious difference between RHOA^{WT} and RHOA^{A161V} was in the spectral region of the Arg and Lys side chains (Supplementary Fig. 11b, c). RHOA^{A161V} is similar to RHOA^{WT}-GMPPNP in both forms, with more missing sidechains and amide cross-peaks. Based on the normalized

https://doi.org/10.1038/s41467-024-51445-z



intensity plot for non-overlapping assigned HNs in all four samples (Fig. 5a), residues that vary the most in intensity are those located in the P-loop, the switch regions, and around the mutation, with the largest intensity change observed for V35 in Switch I. Like the activated RHOA^{WT}-GMPPNP, RHOA^{A161V} in both states showed reduced intensities in these regions compared with RHOA^{WT}-GDP, indicating slower timescale motions.

Chemical shift perturbations (CSPs) of the assigned HNs were calculated to allow detailed analysis of conformational changes (Fig. 5b). We first compared RHOA^{WT} vs. RHOA^{A161V} in the same nucleotide-bound state (Fig. 5b, yellow and purple dots; Supplementary Fig. 16a, b). As expected, the A161V mutant did not exhibit an A161 amide peak in the spectrum. Other changes around the site of the mutations included shifted resonances for residues either flanking

Fig. 5 | RHOA^{A161V}-GDP showed a population of active conformation in the ^{1}H-^{15}N HSQC spectra. a Plot of peak intensities against residue number for non-overlapping assigned peaks. Intensities were normalized to the average peak intensity from assigned, non-overlapping peaks in the RHOA^{WT}-GDP spectrum. The domain structure of truncated RHOA (residues 1–181) is aligned at the top of the plot and the red asterisk (*) is the mutational site. **b** Plot of CSPs for assigned peaks against residue number. For V38 and S160, the "active" peak (most similar to RHOA^{WT}-GMPPNP) in the RHOA^{A161V}-GDP spectrum was used to calculate the CSPs. **c** ^{1}H-^{15}N HSQC spectra of GDP- and GMPPNP-bound RHOA^{WT} and RHOA^{A161V} indicated that RHOA^{A161V}-GDP had two populations, as exemplified by residue V38 (top panel) and S160 (bottom panel). **d** Average intensities of ^{1}H-^{15}N HSQC spectra, normalized to the corresponding RHOA samples prior to RHOTEKIN addition, were plotted against ratios of titrated RHOTEKIN-RBD to RHOA. The error bars are the standard deviation of the averaged intensities. **e** Titration of 2X RHOTEKIN-RBD to RHOA^{A161V}-GDP indicated that for the doubled peaks for V38 (left panel) and S160 (right panel). Black: apoprotein; Red: with 2X RHOTEKIN-RBD. **f** Titration curve of peak intensities for V38. The error bars are the same as in **d**. The "active" peak (solid black curve) in RHOA^{A161V}-GDP had a greater decrease in intensity upon binding than the other (dotted black curve). In **d** and **f**, the spectrum of each sample at each condition was collected once. Source data are provided as a Source Data file.

(S160 and T163, containing the SAK motif) or lying close to the mutation (residues G116, K119, D120, L121, and R122, containing the N/TKxD motif). The largest CSPs between RHOA^{WT} and RHOA^{A161V} were observed in the P-loop and the switch regions. Combining the intensity and CSP analyses (Fig. 5a, b), it is clear that a single A161V mutation influences the dynamics and conformation of the P-loop and switch regions. This is not surprising, as the SAK and N/TKxD motifs are known to have long-range allosteric effects on small GTPase activity[31].

We further examined the key residues that underwent conformational changes in RHOA^{WT} upon nucleotide exchange and the effect of A161V. CSP comparisons of RHOA^{WT}-GDP vs. RHOA^{WT}-GMPPNP showed that most of the changes occurred in amides located in the P-loop and preceding region, the switch regions, and amides in the α3/L7 region (Fig. 5b, green dots; and Supplementary Fig. 16c). The α3/L7 region (residues 90-110) is known to drive switch region motion[32]. Similar changes were observed for the CSPs between RHOA^{A161V}-GDP and RHOA^{A161V}-GMPPNP (Fig. 5b, blue dots; and Supplementary Fig. 16d). Interestingly, when comparing all four samples for these key residues, we found that A161V affected most of the key residues. Although the CSPs of RHOA^{A161V}-GDP vs RHOA^{WT}-GMPPNP (Supplementary Fig. 17a, cyan dots) were generally larger than the CSPs of RHOA^{A161V}-GDP vs. RHOA^{WT}-GDP (Supplementary Fig. 17a, yellow dots), RHOA^{A161V}-GDP displayed decreased intensity for residues in the switch regions, similar to RHOA^{WT}-GMPPNP (Fig. 5a). Most of the observable Switch II residues moved in the direction of RHOA^{WT}-GMPPNP, including T60, E64, Y66, R68, S73, and Y74 (Supplementary Fig. 17b). Q29 was missing in both GDP- and GMPPNP-bound RHOA^{A161V}, differing from a previous study in which the Q29 peak shifted with different nucleotides[30].

A particularly interesting observation was the amide cross-peak of V38 (Fig. 5b, c). This peak shifted significantly between GDP- and GMPPNP-bound RHOA^{WT}, making it a good indicator of active versus inactive states. Interestingly, there are two peaks for V38 in GDP-bound RHOA^{A161V} with shifts similar to those of the two states, indicating that it has two distinct populations. In a model of the RHOA/RHOTEKIN-RBD complex generated by AlphaFold2[33,34], V38 is located at the interaction surface (Supplementary Fig. 18a). Another example is S160 (Fig. 5c). In addition, we observed NOESY differences in V35 HN (Supplementary Fig. 18b). The chemical shifts of the Y34 Hβs and V35 methyl groups differed between RHOA^{WT} and RHOA^{A161V}, indicating changes in the chemical environment of the Switch I region. Further investigation is warranted to fully understand the implications of these observations.

We also collected ^{1}H-^{15}N HSQC spectra with the RHOA effector, RHOTEKIN, titrated at increasing ratios of RHOA: RHOTEKIN of 0.2, 0.5, 1, and 2. Supplementary Fig. 19a shows the comparison of the spectra of each protein alone or with 2x RHOTEKIN titrated, except for RHOA^{A161V}-GMPPNP, which was titrated with 1x RHOTEKIN, as the 2x RHOTEKIN titration sample had low-intensity peaks (see Fig. 5d). In contrast to RHOA^{WT}-GDP, which showed the least peak intensity changes after titration with RHOTEKIN, the other three samples showed an increased peak intensity reduction (Fig. 5d and Supplementary Fig. 19b). At residues V38 and S160, titration of RHOTEKIN to RHOA^{A161V}-GDP showed a significant intensity reduction for the corresponding "active" peaks similar to that of GMPPNP-bound RHOA^{A161V} (Fig. 5e, f), further supporting the conclusion that RHOA^{A161V}-GDP has an active population capable of directly interacting with effector proteins.

Discussion

In this study, we have examined mutational hotspot A161 of RHOA, which lies within the SAK motif, a highly conserved key element for nucleotide binding in small GTPases. A COSMIC database[21] search revealed at least 11 cases of A161V and two cases of A161P of RHOA mutations in the T cell leukemia/lymphoma patients, whereas equivalent mutations in KRAS, NRAS, and RAC1 appear more frequently. We have applied a combined biochemical, MD simulation, and structural biology approach to reveal the distinct activation mechanisms of these two oncogenic mutant forms of RHOA. Moreover, we have found that these RHOA mutants contain unique conformations and display more than the expected fast-cycling phenotype, capable of interacting with effectors independent of GTP binding. The derived mechanism may have broad implications beyond RHOA, potentially applicable to other GTPases, adding to the well-known mechanism of action of mutations like KRAS-G12C which has become targetable after decades of mechanistic studies.

Both RHOA^{A161P} and RHOA^{A161V} displayed increased binding to RHOGEF and an increased rate of nucleotide exchange. The two mutants drive fast cycling via different mechanisms. RHOA^{A161P} had an altered interaction with the guanine nucleotide base in the crystal structure but had only small conformational changes around the nucleotide phosphate groups (GDP or GTP) based on ^{31}P NMR spectra. RHOA^{A161V}, as well as RHOA^{F30L}, on the other hand, displayed significant conformational changes based on the interpretation of the ^{31}P resonance shifts in both GDP- and GTP-analog-bound states – RHOA^{A161V}-GDP and RHOA^{F30L}-GDP showed a state with open nucleotide-binding pocket and RHOA^{A161V}-GTPγS and RHOA^{F30L}-GTPγS shift towards some inactive states with open Switch I. Moreover, RHOA^{A161V} had an increased solvent-accessible area near GDP in the crystal structure, and subsequent MD simulations supported a more open Switch I. Consistently, GTPγS-bound RAC1 F28L showed an increased solvent-accessible area for the nucleotide (1084.75 Å^2, PDB ID 4GZM)[35], than GMPPNP-bound RAC1 WT (896.09 Å^2, PDB ID 3TH5)[36]. Another fast-cycling mutant, KRAS4B^{A146T} (A146 in KRAS is equivalent to A161 in RHOA), exists in an open conformation with a pronounced extension of Switch I and β2 away from the body of the protein and loses Mg^{2+} coordination when GDP-bound (PDB ID 6BOF)[37].

Strikingly, we found that both RHOA^{A161P}-GDP and RHOA^{A161V}-GDP interacted with effectors. There are several lines of supporting evidence: (1) effector pull-down assays, (2) ^{31}P NMR of RHOA^{A161V}-GDP titrated with GST-RHOTEKIN-RBD, (3) ^{1}H-^{15}N HSQC spectra of RHOA^{A161V}-GDP with/without RHOTEKIN-RBD. This effector binding in the GDP state seems unrelated to the conformation equilibrium of RHOA-GTP. With mutations reducing affinity around the guanine base (like A161P) or opening the nucleotide-binding pocket (like A161V), GDP could slide and fill the phosphate binding pocket, mimicking GTP binding. However, this cannot explain why RAC1^{P29S} and RAC1^{A159V} do not behave the same. It is also possible that those mutations, especially A161V, which shows slower timescale motions in NMR, increase the

energy barrier between the GDP-bound states, trapping RHOA in more conformational states, including inactive and active states. Indeed, both GDP-bound $RHOA^{A161V}$ and $RHOA^{A161P}$ are more structurally heterogeneous than $RHOA^{WT}$, based on MD simulations.

Some GDP-bound small GTPase proteins have been observed to bind to downstream effectors. For example, RAS-GDP interacts with mutants of RAF[38]. Switch I, but not Switch II, in the RAS-GDP/RAF mutant complex, was found in a conformation similar to RAS-GTP[39]. In addition, there are two interesting cases in the PDB databank that GDP- and GTP analog-bound RHO adopt similar conformation when complexed with the same partner protein: RAC1-GDP or RAC1-GMPPNP with ARFAPTIN[40], and RHOA-GDP or RHOA-GTPγS with TRPV4[41]. In both cases, Switch I adopts an open conformation. RHOE mutants G23V and T25N in *Dictyostlium*, the equivalent of RHOA G17V and T19N, induced AKT phosphorylation in cells and directly activated mTORC2-mediated AKT phosphorylation in a GDP-bound form in vitro[42]. The possibility that RHOA G17V could be active in the GDP-bound form is interesting and can explain why seemingly gain-of-function mutations (A161V, A161P, C16F, and C16R) and loss-of-function mutations (G17V and A161E) can co-exist in the same cancer type – they all lead to signaling events. The activation of mutants in the GDP-bound form is likely not specific to RHOA. Mutations resulting in an "active" state have also been suggested by an MD study using principal component analysis (PCA) of $KRAS4B^{G12V}$-GDP[43]. It visits the active state more frequently than $KRAS4B^{G12D}$-GDP[44]. Our studies of the tumor-derived RHOA mutations highlight the possibility that GDP-bound mutant GTPases are also critical signaling molecules and targeting them in the GDP-bound state is equally important. Further exploration of RHOA in structural dynamics and its differences from other RHO GTPases and RAS could shed light on the unique mechanisms of widespread mutations in RHOA.

Decoding the molecular dynamics and conformational equilibrium of RHO GTPases to predict their biological properties is challenging because of their inherent conformational heterogeneity. A general principle cannot be established yet based on current studies. Increased state 1 in the GTP-bound state does not correlate with reduced affinity for effectors, nor increased nucleotide exchange. Nonetheless, oncogenic mutants, even at the same residue, were characterized by distinct conformational landscapes. These changes are almost impossible to address in vivo and therefore, in this study, we relied heavily on biophysical in vitro methods and computational MD simulations. The importance of studies on conformational space and dynamics was exemplified by the successful development of KRAS-G12C covalent inhibitors, which eventually led to the FDA-approved sotorasib (AMG510) and adagrasib (MRTX849)[45,46]. The targeted pocket, as well as other main ligand-binding pockets on RAS, are not readily observed in the absence of compound binding. Understanding the unique conformations observed in the mutants and exploiting the ensembles of RAS and RHO in both GDP- and GTP-bound states can facilitate the identification of target sites of various mutant-specific conformers.

Methods

Protein expression and purification

Plasmid encoding human full-length RHOA in pGEX-2T vector was a gift from Jonathan Chernoff (Addgene plasmid # 12202). It was used to introduce a stop codon at residue 182 and the F25N mutation using QuickChange Lightning Site-Directed Mutagenesis Kit (Agilent, Santa Clara, CA) according to manufacturer's instructions, resulting in a construct encoding human RHOA residue 1-181 and contains F25N mutation ($pGEX\text{-}RHOA^{\Delta C, F25N}$). The F25N mutation is known to stabilize the expression of RHOA in bacteria and is commonly used in RHOA constructs for structural studies. For simplicity, we refer to this construct as $RHOA^{WT}$ throughout the paper. Additional mutations A161P, A161V, T37A, or F30L were further introduced based on $RHOA^{WT}$ ($RHOA^{A161P}$, $RHOA^{A161V}$, $RHOA^{T37A}$ and $RHOA^{F30L}$). Plasmid encoding human full-length RAC1 in pGEX-2T vector was from the lab archive and mutations P29S and A159V were introduced using QuickChange Lightning Site-Directed Mutagenesis Kit. Sequences of mutagenesis primers and catalog numbers of key reagents in this study are included in Supplementary Data 1.

RHOA proteins were expressed in *Escherichia coli* (*E. coli*) BL21 (DE3) strain (New England Biolabs) with an N-terminal GST tag cleavable by the thrombin protease. The cells were grown in LB media with 100 μg/mL Ampicillin and induced at $A_{600} = 0.8$ with 0.2 mM isopropyl β-D-1-thiogalactopyranoside (IPTG) overnight at 20 °C. The cells were harvested by centrifugation, resuspended in buffer A (25 mM Hepes pH7.4, 1 M NaCl, 5 mM $MgCl_2$, 5 μM GDP), supplemented with 1 mM phenylmethylsulfonyl fluoride (PMSF), 10 mM DTT and then sonicated. The supernatant was then put through the GST-affinity column (GSTrap FF, Cytiva), washed with buffer A, followed by cleavage of the GST tag with thrombin (Sigma) on column in cleavage buffer (50 mM Hepes pH7.4, 150 mM NaCl, 10 mM $MgCl_2$, 2.5 mM $CaCl_2$) for 1 hour at room temperature. Cleaved RHOA proteins were then eluted out with buffer A, followed by a final purification step using size-exclusion chromatography (HiLoad 16/600 Superdex 200 pg, Cytiva) with 20 mM Tris pH7.5, 100 mM NaCl, 5 mM $MgCl_2$, and 1 mM DTT. The protein samples were concentrated using centrifugal filters with a molecular weight cutoff of 10 KDa, and the concentrations of the proteins were subsequently measured by Bradford assay. Purified RHOA proteins are GDP-bound, as confirmed by ^{31}P-NMR. To obtain RHOA-GTP, RHOA bound-GDP was exchanged to non-hydrolyzable GTP analog GMPPNP (Sigma) or slow-hydrolyzable GTP analog GTPγS (Sigma) using alkaline phosphatase coupled to agarose beads (Sigma) as previously described[47]. Briefly, RHOA-GDP, 10-fold GTP analogs, and CIP beads were rotated in ~1 mL buffer containing 40 mM Tris pH7.5, 200 mM $(NH_4)_2SO_4$, 10 μM $ZnCl_2$, 5 mM DTT overnight at 4 °C. After exchange, the supernatant was subjected to size-exclusion chromatography. The presence of GMPPNP or GTPγS was confirmed by ^{31}P-NMR. RAC1 proteins were purified similarly.

RHOTEKIN RBD (residues 7-89), ROCK2 RBD (residues 945-1096), p190 GAP domain (residues 1-251), and PAK1 RBD (residues 67-150) were constructed in pGEX-KG vector and were expressed as described above for RHOA. The cells were harvested by centrifugation, resuspended in buffer B (25 mM Hepes pH7.4, 1 M NaCl), supplemented with 1 mM PMSF, 10 mM DTT, and then sonicated. The supernatant was then put through a GST-affinity column (GSTrap FF, Cytiva), washed with buffer B, then eluted in 100 mM Tris-HCl pH8.0, 150 mM NaCl, and 10 mM reduced glutathione. Eluted proteins were then purified by size-exclusion chromatography (HiLoad 16/600 Superdex 200 pg, Cytiva) with 20 mM Tris pH7.5, 100 mM NaCl, and 1 mM DTT. The protein samples were concentrated using centrifugal filters with a molecular weight cutoff of 30 KDa, and the concentrations of the proteins were subsequently measured by Bradford assay.

A modified pMAL vector ($pMALc2H_{10}T$) expressing LARG DH/PH fragment (residues 766–1139) was obtained from Dr. John Tesmer (Dept. Chemistry and Biochemistry, The University of Texas at Austin). The $pMALc2H_{10}T$ expression vector was generated by inserting oligonucleotides encoding a decahistidine (H_{10}) tag followed by a TEV protease recognition site between AvaI and EcoRI of the pMALc2X vector (New England Biolabs)[48]. Expression and purification of MBP-LARG-DH/PH were carried out as previously described[49] but without the TEV cleavage step. Briefly, MBP-LARG-DH/PH protein was expressed in *E. coli* BL21 (DE3) strain (New England Biolabs). The cells were grown in LB media with 100 μg/mL Ampicillin and 0.2% glucose, induced at $A_{600} = 0.8$ with 0.2 mM IPTG overnight at 20 °C. After standard affinity chromatography for His-tagged proteins using Histrap FF column (Cytiva), the MBP-LARG-DH/PH fusion protein was further cleaned up using size-exclusion chromatography (HiLoad 16/

600 Superdex 200 pg, Cytiva) with 20 mM Tris pH7.5, 100 mM NaCl, and 1 mM DTT.

GST pull-down assays

Purified GST-RHOTEKIN-RBD, GST-ROCK2-RBD, GST-p190-GAP, and MBP-LARG-DH/PH were used to pull down RHOA proteins. For GST-fusion proteins, approximately 20 µg of each GST-fused protein was immobilized on agarose-glutathione beads (Sigma) by incubating 30 min at 4 °C, washed three times in a buffer containing 50 mM Hepes (pH 7.4), 100 mM NaCl, 5 mM $MgCl_2$, 0.3% Triton-X100, 1 mM DTT, 10 µM GDP or GMPPNP, and then mixed with 5 µg of purified RHOA proteins for 1 h at 4 °C. For MBP-LARG-DH/PH, approximately 10 µg protein was immobilized on amylose resin (New England Biolabs) by incubating 30 min at 4 °C, washed three times in a buffer containing 50 mM Hepes (pH 7.4), 100 mM NaCl, 0.3% Triton-X100, 1 mM DTT, 5 mM EDTA or 5 mM $MgCl_2$, with or without 10 µM GDP or GMPPNP, and then mixed with 2 µg of purified RHOA proteins for 1 h at 4 °C. For both cases, after incubation, beads were washed three times with the same buffer, boiled with loading buffer at 95 °C for 5 min to elute the beads. The eluted mixtures were then subjected to 4–15% SDS-PAGE and transferred to PVDF for Western blot analysis using anti-RHOA antibody (Cell signaling Technology). The immune complexes were visualized by using chemiluminescence reagents (Bio-RAD). The GST-RHOTEKIN-RBD, GST-ROCK2-RBD, GST-p190-GAP, or the MBP-LARG-DH/PH input were obtained by stain-free imaging of the gel before transfer. Purified GST-PAK1-RBD was used to pull down RAC1 proteins with similar protocols with 10 µg GST-PAK1-RBD immobilized and 1 µg RAC1 proteins used.

Microscale thermophoresis (MST) binding assay

A NanoTemper Monolith Instrument (NT.115) was used for measuring thermophoresis. In this instrument an infra-red Laser (IR-Laser) beam couples into the path of light (i.e., fluorescence excitation and emission) with a dichroic mirror and is focused into the sample fluid through the same optical element used for fluorescence imaging. The IR laser is absorbed by the aqueous solution in the capillary and locally heats the sample with a $1/e^2$ diameter of 25 µm. Up to 24 mW of laser power where used to heat the sample, without damaging the biomolecules[50]. RHOA proteins were labeled using Maleimide labeling kit (NanoTemper Technologies, Germany) according to the manufacturer's protocol Thermophoresis of the RHOA proteins in the presence of varying concentrations of RHOTEKIN-RBD was analyzed for 30 s. Measurements were performed at room temperature and standard deviation was calculated from three or more independent experiments. Data were normalized to ΔFnorm [‰] (10*(Fnorm(-bound) - Fnorm (unbound))). The dissociation constant (K_D) was obtained by nonlinear regression fit using a one-site specific binding model for $RHOA^{WT}$, and a two-site specific binding model for $RHOA^{A161P}$ and $RHOA^{A161V}$ in Prism (version 9.3.1, GraphPad Software).

Nucleotide dissociation assays

500 nM purified GDP-bound RHOA proteins in buffer containing 20 mM Tris-HCl pH 7.5, 100 mM NaCl, and 1 mM EDTA were incubated with 250 nM of BODIPY FL-GDP (Invitrogen) at 25 °C for about 2 h, then $MgCl_2$ was added to a final concentration of 5 mM. The baseline of the fluorescence signal was then monitored for 10 mins and made sure to be constant. For exchange, 5 µM GMPPNP (10-fold) was added in the presence of 5 mM $MgCl_2$ or 10 mM EDTA. Fluorescence intensity changes were monitored at 1-minute intervals for about 30 min using an EnVision Multimode Plate Reader (Perkin Elmer) with excitation/emission wavelengths of 485 and 535 nm. For data processing, the fluorescence intensities after adding free GMPPNP were subtracted by buffer baseline reading and then normalized as percentages of the baseline reading subtracted by buffer baseline reading, plotted against time. Standard deviation was calculated from four or more independent experiments. For most cases, nonlinear regression and the dissociation-one phase exponential decay model were used to obtain the pseudo first-order rate constant using Prism (GraphPad Software). The exception is for $RHOA^{F30L}$, $RHOA^{A161P}$, and $RHOA^{A161V}$ dissociation under EDTA condition, nonlinear regression and the two-phase decay model were used to obtain the pseudo first-order rate constant.

Nucleotide association assays

For association, 25 µL 0.2 µM BODIPY-FL-GDP (Invitrogen) in a buffer containing 20 mM Tris-HCl pH 7.5, 100 mM NaCl, and 5 mM $MgCl_2$ was monitored for 10 minutes as fluorescence baseline using an EnVision Multimode Plate Reader (Perkin Elmer) with excitation/emission wavelength of 485 and 535 nm. 25 µL 2 µM purified GDP-bound RHOA proteins in the same buffer were then added and fluorescence intensity changes were monitored at 1-minute intervals for about 30 min. For data processing, the fluorescence intensities after adding RHOA proteins were subtracted by the baseline reading and then normalized as percentages of the same baseline reading and plotted against time. The standard deviation was calculated from ten independent experiments. Curves were fitted with nonlinear regression and the one-phase association model to obtain the pseudo first-order rate constant using Prism (GraphPad Software). The resulting pseudo first-order dissociation and association rates are summarized in Supplementary Table 1. The rates were compared between proteins using unpaired t-tests in Prism.

GTPase activity assay

Intrinsic and GAP-stimulated RHOA GTPase activities were measured using the GTPase-Glo™ Assay (Promega) according to the manufacturer's protocol. For intrinsic GTPase assay, 1µg of GDP-bound RHOA proteins was incubated with 5 µM GTP substrate in 10 µL GTPase/GAP reaction buffer (50 mM Tris-HCL, pH7.5, 50 mM NaCl, 20 mM EDTA, and 5 mM $MgCl_2$) for various time points at room temperature. Upon completion of the GTPase reaction, equal amount of GTPase-Glo reagent (10 µL) is added and incubated with shaking for 30 min at room temperature. The GTPase-Glo reagent contains an enzyme that converts the remaining GTP to ATP. Subsequently, 2-fold amount of detection reagent (20 µL) is added to detect the ATP generated. After 5–10 min at room temperature, luminescence signal is read using an EnVision Multimode Plate Reader (Perkin Elmer). For dose responding curves, reactions were assembled with various amounts of wildtype and mutant RHOA proteins in the GTPase/GAP buffer without or with the presence of 2 µM GST-p190-GAP and incubated for 1 h at room temperature. Each experiment was repeated for at least four times. For hydrolysis rate experiments, the luminescence reading was normalized as percentage of buffer control and fitted with nonlinear regression and the dissociation-one phase exponential decay model with constraints $K_0 = 100$, plateau between 0 and 10% to obtain the pseudo first order rate constants using Prism. For dose titration experiments, luminescence reading was normalized as percentage of the maximum luminescence reading of the same protein and fitted with nonlinear regression and the [inhibitor] vs. response model with constraints IC50 > 0 to obtain the EC50, which is the concentration of RHOA to produce 50% of maximum hydrolysis of 5 µM GTP substrate[26]. The hydrolysis rate and EC50 were compared between proteins using unpaired t-tests in Prism.

Crystallization, structure determination, and refinement

Crystals of $RHOA^{A161P}$ and $RHOA^{A161V}$ in complex with GDP were grown by hanging drop method in a 1:1 volume ratio of purified RHOA proteins and reservoir solution containing 0.1 M Tris-HCl (pH8.3), 16–20% PEG 8000, and 15% (v/v) 1,4-dioxane at 277 K. Crystals were equilibrated in a cryoprotectant buffer containing reservoir buffer with 30% (v/v) PEG 8000 and were flash-frozen in liquid nitrogen. X-ray data

were collected with a wavelength of 0.97931 Å at 100 K using Beamline 31-D-D at the Advanced Photon Source (APS). The datasets were indexed and integrated using Mosflm (version 7.2.0)[51] and Scala (version 3.3.22)[52]. The structures of RHOA^{A161P} and RHOA^{A161V} in complex with GDP were determined by molecular replacement with the program Phaser[53] using a searching model based on the structure of RHOA-GDP (PDB ID 1FTN)[54], Refinement was performed using PHENIX (version 1.19.2)[55] and models were built with COOT (version 0.8.9.2)[56] in alternative rounds. 97.74% and 98.31% of residues are Ramachandran favored, and 2.26% and 1.69% of residues are Ramachandran allowed in final models of RHOA^{A161P}-GDP and RHOA^{A161V}-GDP, respectively. In the structures of RHOA^{A161P} and RHOA^{A161V}, the Switch I region is relatively better defined compared to the previous RHOA^{WT}-GDP crystal structure. Residues in the Switch I region were rebuilt on their omit map individually. In both structures, the Switch II region is well defined. The additional GS insert in the N-terminus and two N-terminal residues of RHOA are missing in the densities implying their disorder. The final model and scaled reflection data were deposited at the PDB (rcsb.org) with code 8FPX for RHOA^{A161P}-GDP and 8FPW for RHOA^{A161V}-GDP. Data collection and refinement statistics are summarized in Supplementary Table 5. Structural figures are generated with PyMOL (version 3.0, Schrödinger, LLC).

^{31}P NMR acquisition

0.5 mL of 0.5–0.8 mM solution of RHOA proteins (GDP-, GMPPNP- or GTPγS-bound) in 20 mM Tris pH7.5, 100 mM NaCl, 5 mM $MgCl_2$, 1 mM DTT, 10% D_2O were used for the NMR data collection. The protein-free nucleotide samples containing approximately 5 mM nucleotide (GDP, GMPPNP, or GTPγS) in the above buffer were used to set up the NMR parameters and served as controls. For experiments on RHOA complexes with effector, GST-RHOTEKIN-RBD was used instead of RHOTEKIN-RBD as the latter has poor stability at higher concentrations during NMR data acquisition. We have previously shown that GST does not affect RHOA ^{31}P NMR spectra[29]. During the titration experiment, GST-RHOTEKIN-RBD was mixed in, and the sample was concentrated back to 0.5 mL using centrifugal filters after 15 min incubation at room temperature.

One-dimensional ^{31}P NMR spectra were acquired at 275 K and 298 K on a Bruker Avance III 600 MHz spectrometer with 5 mm, BBI room temperature probe or BBO Prodigy probe (Bruker Analytik, Rheinstetten, Germany) with a total spectral width of 50 ppm for GDP- and GMPPNP-bound RHOA proteins or 100 ppm for GTPγS-bound RHOA proteins. NMR spectrometer is calibrated every week using 0.1 mM TSP in 10% D_2O as standard with its 1H peak set to 0.0 ppm. Each probe temperature change was monitored for 10 min minimum to ensure stability. Before data collection, the sample was inserted and its temperature was stabilized for a minimum of 10 min; the signal was locked with H_2O and D_2O, tuned and matched on the ^{31}P channel, and shimmed. The data was acquired using 1D pulse program "zgpg30" from Bruker pulse library with the following parameters: time domain (TD) = 30k, DS = 8, acquisition time (AQ) = 0.6 s, relaxation delay (D1) = 3 s, and adjusted number of scans (NS) depending on the sample concentration. For our samples, NS ranges from 1k to 8k. All spectra were acquired, processed, phased, and baseline-corrected using Topspin (version 4.0.3) software (Bruker). For spectral comparison, all spectra were aligned with the inorganic phosphate Pi peak, which was likely coming from GTPγS degradation or impurities from the guanine nucleotides.

^{1}H-^{15}N HSQC NMR acquisition

To obtain ^{15}N-labeled RHOA for ^{1}H-^{15}N HSQC NMR experiments, bacterial cells were grown in M9 minimal medium with $^{15}NH_4Cl$ as the sole nitrogen source. Purified RHOA proteins were GDP-bound. GMPPNP- and GTPγS-bound RHOA proteins were obtained by nucleotide exchanging using alkaline phosphatase coupled to agarose beads (Sigma)[29,57]. NMR samples with a final volume of 0.5 mL were made with 0.4–0.6 mM RHOA in 20 mM Tris pH 7.5, 100 mM NaCl, 5 mM $MgCl_2$, 1 mM DTT, 10% D_2O, and 2 mM GDP, GMPPNP, or GTPγS in 5 mm Shigemi tubes. RHOTEKIN-RBD was used for the effector titration experiments, as ^{1}H-^{15}N HSQC spectra data collection took ~1 h compared to the less sensitive ^{31}P NMR spectra that took 3–12 h each. The smaller molecular weight of the RHOA/RHOTEKIN-RBD complex resulted in a better signal-to-noise ratio than the RHOA/GST-RHOTEKIN-RBD complex.

All data were collected at 298 K on a Bruker Avance III 600 MHz spectrometer with a 5 mm BBO Prodigy probe. Pulse program "hsqcetfpgpsi2" from Bruker pulse library was used for ^{1}H-^{15}N HSQC experiments with the following parameters: spectral width (SW) = 20.0 ppm (H) and 51.4 ppm (N), acquisition time (AQ) = 42.6 ms (H) and 20.5 ms (N), relaxation delay (D1) = 2 s, number of scans (NS) = 8. 3D-NOESY data were collected with the pulse program "noesyhsqcf3gpsi3d" from Bruker pulse library with the same ^{15}N-labeled samples. The parameters were mixing time = 100 ms, relaxation delay (D1) = 1 s, and number of scans (NS) = 8. For H(N), N, H dimensions, spectral width (SW) = 20.0, 51.4, and 14.0 ppm, acquisition time (AQ) = 42.6, 14.4, and 15.2 ms.

GDP- and GMPPNP-bound RHOA^{WT} amide HN chemical shifts were assigned by comparison with published RHOA$^{\Delta C}$ peak assignments (BMRB ID 16668 and 16669)[30] and confirmed by comparisons of sequential ^{15}N NOESY strips. RHOA^{A161V} assignments were made by comparing ^{15}N NOESY strips with those of GDP- and GMPPNP-bound RHOA^{WT}. The buffer condition of BMRB 16668 and 16669 (20 mM HEPES buffer, 100 mM NaCl, 5 mM $MgCl_2$, 2 mM TCEP, 10% D_2O, pH 7) was very close to ours. We were able to transfer assignments for 68.8%, 61.8%, 52.9%, and 52.9% of HNs in RHOA^{WT}-GDP, RHOA^{WT}-GMPPNP, RHOA^{A161V}-GDP, and RHOA^{A161V}-GMPPNP, respectively. The intensities of the non-overlapping assigned peaks for all four ^{1}H-^{15}N HSQC spectra were normalized to the average peak intensity for each spectrum (Fig. 5a). For the RHOTEKIN titration experiments, peak intensity changes for all non-overlapping residues of RHOA titrated with RHOTEKIN at various ratios were normalized (I/I_o) by dividing the peak intensities in the corresponding RHOA samples prior to the addition of RHOTEKIN (Fig. 5d and Supplementary Fig. 19b). The CSPs for Fig. 5b and Supplementary Fig. 17a were calculated using the formula $\Delta\delta$ (ppm) $= \sqrt{0.5 \times \left[\left(\frac{\Delta\delta H}{2.56}\right)^2 + \left(\frac{\Delta\delta N}{0.54}\right)^2\right]}$[58]. NMRFAM-SPARKY (version 3.115)[59] was used for peak assignment and Topspin (version 4.0.3, Bruker) was used for data acquisition and processing.

MD simulation

All simulations were performed according to the protocol described in our previous studies[60–62]. The updated CHARMM program with the modified all-atom force field (version 36 m)[63–65] was utilized in the MD simulations on RHOA-GDP systems in explicit solvent. CHARMM is a biomolecular simulation program that has gained considerable traction within the scientific community due to its ability to perform atomic-level simulations of various biomolecular systems. The small GTPase RHOA proteins have well-defined crystal structures for both the wild type and its mutants, which are currently available for analysis. Our MD simulations utilized the crystal structures of the catalytic domain of GDP-loaded RHOA^{WT} (PDB ID 6V6U), RHOA^{A161P} (PDB ID 8FPX), and RHOA^{A161V} (PDB ID 8FPW). For all systems, the F25N mutation was retained for consistency with the experimental data.

The initial RHOA configurations were solvated using the TIP3P model in an isometric unit cell box of 90 × 90 × 90 Å^3; 51 Na^+ and 43 Cl^- ions were added to the simulation systems to neutralize the system with a final concentration of 100 mM NaCl. The simulation system contains approximately 74,000 atoms, including approximately 24,000 water molecules. The solvent was included in 10,000 steps of

minimization and 50,000 steps of dynamic cycles with a step size of 2 fs and most backbone atoms were constrained. Here, no constraints were applied to N25 or the surrounding residues to let it stabilize. Next, the harmonic constraints were gradually lifted with long-range electrostatic calculations using the particle mesh Ewald (PME) method. The simulation was controlled at 310 K with Langevin temperature control and at 1 atm with Nosé–Hoover Langevin piston method. The production runs for the systems, each with a 1 µs duration, were completed using Nanoscale Molecular Dynamics (NAMD, version 2.13)[66] parallel-computing code under the NPT ensemble (constant number of atoms, pressure, and temperature). It has been argued that in general, µs simulation time frames may not be sufficient to observe real-time protein dynamics. Here, the production runs of µs were sufficient to sample the ensembles of conformations since these RHOA systems quickly reached equilibrium within the simulation time frame. In addition to the primary set of simulations, two supplementary sets of simulations were conducted for the same systems to assess reproducibility. Our findings indicated that the results were consistent between replicates, thereby providing evidence of the reproducibility of the critical results (Supplementary Fig. 20). Thus, the statistical data presented here were derived from the primary set of simulations. The RHOA systems typically reached equilibrium after 50 ns (Supplementary Fig. 8a), and thus averages were taken afterward. All simulations were performed using the Biowulf cluster at the National Institutes of Health (Bethesda, MD, USA). VMD (version 1.9.4)[67] and Chimera (version 1.13.1)[68] were used to analyze the simulation systems. RHOA coordinates of the starting points and representative relaxed conformations for $RHOA^{WT}$, $RHOA^{A161P}$, and $RHOA^{A161V}$ are included in Supplementary Data 2.

Statistics and reproducibility

All biochemical assays are carried out for at least three independent repeats. Statistical analyses were performed using unpaired t-tests in Prism (GraphPad Software). No statistical method was used to predetermine the sample size. No data were excluded from the analyses.

Reporting summary

Further information on research design is available in the Nature Portfolio Reporting Summary linked to this article.

Data availability

The final models and scaled reflection data for $RHOA^{A161P}$-GDP and $RHOA^{A161V}$-GDP have been deposited in the PDB database (rcsb.org) under accession codes 8FPX and 8FPW, respectively. The amide ^{1}H and ^{15}N assignments of GDP- and GMPPNP-bound $RHOA^{WT}$ and $RHOA^{A161V}$ were deposited in the Biological Magnetic Resonance Data Bank (BMRB) with accession ID 51804 for $RHOA^{WT}$-GDP, 51805 for $RHOA^{WT}$-GMPPNP, 51806 for $RHOA^{A161V}$-GDP, and 51807 for $RHOA^{A161V}$-GMPPNP. Source data are provided with this paper. Other structural data used in this study are available in the PDB or BMRB database under the following accession codes:6V6U (crystal structure of $RHOA^{WT}$-GDP, construct contains residues 1-181, with F25N mutation to improve expression) 6V6M (crystal structure of $RHOA^{WT}$-GMPPNP, construct contains residues 1-181, with the F25N mutation to improve expression) 4GZM (crystal structure of $RAC1^{F28L}$-GTPγS, construct contains residues 2-177) 3TH5 (crystal structure of RAC1-GMPPNP, construct contains residues 2-177) 6BOF (crystal structure of $KRAS^{A146T}$-GDP, construct contains residues 2-169, with additional mutations R152G, E154D, Q166K, Y167H, R168K, and L169E) 1FTN (crystal structure of RHOA-GDP, construct contains F25N mutation to improve expression) 16668 (assigned chemical shifts of RHOA-GDP, construct contains residues 1-181) 16669 (assigned chemical shifts of RHOA-GTPγS, construct contains residues 1-181) Source data are provided with this paper.

References

1. Etienne-Manneville, S. & Hall, A. Rho GTPases in cell biology. *Nature* **420**, 629–635 (2002).
2. Hodge, R. G. & Ridley, A. J. Regulating Rho GTPases and their regulators. *Nat. Rev. Mol. cell Biol.* **17**, 496–510 (2016).
3. Haga, R. B. & Ridley, A. J. Rho GTPases: Regulation and roles in cancer cell biology. *Small GTPases* **7**, 207–221 (2016).
4. Vetter, I. R. & Wittinghofer, A. The guanine nucleotide-binding switch in three dimensions. *Science* **294**, 1299–1304 (2001).
5. Cherfils, J. & Zeghouf, M. Regulation of small GTPases by GEFs, GAPs, and GDIs. *Physiol. Rev.* **93**, 269–309 (2013).
6. Li, H., Peyrollier, K., Kilic, G. & Brakebusch, C. Rho GTPases and cancer. *Biofactors* **40**, 226–235 (2014).
7. Orgaz, J. L., Herraiz, C. & Sanz-Moreno, V. Rho GTPases modulate malignant transformation of tumor cells. *Small GTPases* **5**, e29019 (2014).
8. Porter, A. P., Papaioannou, A. & Malliri, A. Deregulation of Rho GTPases in cancer. *Small GTPases* **7**, 123–138 (2016).
9. Wang, K. et al. Whole-genome sequencing and comprehensive molecular profiling identify new driver mutations in gastric cancer. *Nat. Genet* **46**, 573–582 (2014).
10. Palomero, T. et al. Recurrent mutations in epigenetic regulators, RHOA and FYN kinase in peripheral T cell lymphomas. *Nat. Genet* **46**, 166–170 (2014).
11. Nagata, Y. et al. Variegated RHOA mutations in adult T-cell leukemia/lymphoma. *Blood* **127**, 596–604 (2016).
12. Sakata-Yanagimoto, M. et al. Somatic RHOA mutation in angioimmunoblastic T cell lymphoma. *Nat. Genet* **46**, 171–175 (2014).
13. Yoo, H. Y. et al. A recurrent inactivating mutation in RHOA GTPase in angioimmunoblastic T cell lymphoma. *Nat. Genet* **46**, 371–375 (2014).
14. Rohde, M. et al. Recurrent RHOA mutations in pediatric Burkitt lymphoma treated according to the NHL-BFM protocols. *Genes Chromosomes Cancer* **53**, 911–916 (2014).
15. Lawrence, M. S. et al. Discovery and saturation analysis of cancer genes across 21 tumour types. *Nature* **505**, 495–501 (2014).
16. Bustelo, X. R. RHO GTPases in cancer: known facts, open questions, and therapeutic challenges. *Biochem. Soc. Trans.* **46**, 741–760 (2018).
17. Schaefer, A. & Der, C. J. RHOA takes the RHOad less traveled to cancer. *Trends Cancer* **8**, 655–669 (2022).
18. Ishikawa, S. Opposite RHOA functions within the ATLL category. *Blood* **127**, 524–525 (2016).
19. Svensmark, J. H. & Brakebusch, C. Rho GTPases in cancer: friend or foe? *Oncogene* **38**, 7447–7456 (2019).
20. Zandvakili, I., Lin, Y., Morris, J. C. & Zheng, Y. Rho GTPases: Anti- or pro-neoplastic targets? *Oncogene* **36**, 3213–3222 (2017).
21. Tate, J. G. et al. COSMIC: the Catalogue Of Somatic Mutations In Cancer. *Nucleic Acids Res.* **47**, D941–D947 (2019).
22. Rittinger, K., Walker, P. A., Eccleston, J. F., Smerdon, S. J. & Gamblin, S. J. Structure at 1.65 A of RhoA and its GTPase-activating protein in complex with a transition-state analogue. *Nature* **389**, 758–762 (1997).
23. Lin, R., Cerione, R. A. & Manor, D. Specific contributions of the small GTPases Rho, Rac, and Cdc42 to Dbl transformation. *J. Biol. Chem.* **274**, 23633–23641 (1999).
24. Spoerner, M., Herrmann, C., Vetter, I. R., Kalbitzer, H. R. & Wittinghofer, A. Dynamic properties of the Ras switch I region and its importance for binding to effectors. *Proc. Natl Acad. Sci. USA* **98**, 4944–4949 (2001).
25. Zhang, B., Zhang, Y., Wang, Z. & Zheng, Y. The role of Mg2+ cofactor in the guanine nucleotide exchange and GTP hydrolysis reactions of Rho family GTP-binding proteins. *J. Biol. Chem.* **275**, 25299–25307 (2000).
26. Mondal, S., Hsiao, K. & Goueli, S. A. A Homogenous Bioluminescent System for Measuring GTPase, GTPase Activating Protein, and

Guanine Nucleotide Exchange Factor Activities. *Assay. Drug Dev. Technol.* **13**, 444–455 (2015).
27. Spoerner, M. et al. Conformational states of human rat sarcoma (Ras) protein complexed with its natural ligand GTP and their role for effector interaction and GTP hydrolysis. *J. Biol. Chem.* **285**, 39768–39778 (2010).
28. Geyer, M. et al. Conformational transitions in p21ras and in its complexes with the effector protein Raf-RBD and the GTPase activating protein GAP. *Biochemistry* **35**, 10308–10320 (1996).
29. Lin, Y., Lu, S., Zhang, J. & Zheng, Y. Structure of an inactive conformation of GTP-bound RhoA GTPase. *Structure* **29**, 553–563 e555 (2021).
30. Gasmi-Seabrook, G. M. et al. Real-time NMR study of guanine nucleotide exchange and activation of RhoA by PDZ-RhoGEF. *J. Biol. Chem.* **285**, 5137–5145 (2010).
31. Mott, H. R. & Owen, D. Allostery and dynamics in small G proteins. *Biochem. Soc. Trans.* **46**, 1333–1343 (2018).
32. Vatansever, S., Gumus, Z. H. & Erman, B. Intrinsic K-Ras dynamics: A novel molecular dynamics data analysis method shows causality between residue pair motions. *Sci. Rep.* **6**, 37012 (2016).
33. Mirdita, M. et al. ColabFold: making protein folding accessible to all. *Nat. Methods* **19**, 679–682 (2022).
34. Jumper, J. et al. Highly accurate protein structure prediction with AlphaFold. *Nature* **596**, 583–589 (2021).
35. Davis, M. J. et al. RAC1P29S is a spontaneously activating cancer-associated GTPase. *Proc. Natl Acad. Sci. USA* **110**, 912–917 (2013).
36. Krauthammer, M. et al. Exome sequencing identifies recurrent somatic RAC1 mutations in melanoma. *Nat. Genet* **44**, 1006–1014 (2012).
37. Poulin, E. J. et al. Tissue-Specific Oncogenic Activity of KRAS(A146T). *Cancer Discov.* **9**, 738–755 (2019).
38. Kiel, C. et al. Improved binding of raf to Ras.GDP is correlated with biological activity. *J. Biol. Chem.* **284**, 31893–31902 (2009).
39. Filchtinski, D. et al. What makes Ras an efficient molecular switch: a computational, biophysical, and structural study of Ras-GDP interactions with mutants of Raf. *J. Mol. Biol.* **399**, 422–435 (2010).
40. Tarricone, C. et al. The structural basis of Arfaptin-mediated cross-talk between Rac and Arf signalling pathways. *Nature* **411**, 215–219 (2001).
41. Kwon, D. H. et al. TRPV4-Rho GTPase complex structures reveal mechanisms of gating and disease. *Nat. Commun.* **14**, 3732 (2023).
42. Senoo, H. et al. Phosphorylated Rho-GDP directly activates mTORC2 kinase towards AKT through dimerization with Ras-GTP to regulate cell migration. *Nat. Cell Biol.* **21**, 867–878 (2019).
43. Grudzien, P., Jang, H., Leschinsky, N., Nussinov, R. & Gaponenko, V. Conformational Dynamics Allows Sampling of an "Active-like" State by Oncogenic K-Ras-GDP. *J. Mol. Biol.* **434**, 167695 (2022).
44. Nussinov, R., Liu, Y., Zhang, W. & Jang, H. Protein conformational ensembles in function: roles and mechanisms. *RSC Chem. Biol.* **4**, 850–864 (2023).
45. Canon, J. et al. The clinical KRAS(G12C) inhibitor AMG 510 drives anti-tumour immunity. *Nature* **575**, 217–223 (2019).
46. Hallin, J. et al. The KRAS(G12C) Inhibitor MRTX849 Provides Insight toward Therapeutic Susceptibility of KRAS-Mutant Cancers in Mouse Models and Patients. *Cancer Discov.* **10**, 54–71 (2020).
47. Smith, S. J. in *GTPase Protocols Methods in Molecular Biology* (eds Manser, E.d. & Thomas, L.) (Humana Press, 2002).
48. Kristelly, R., Gao, G. & Tesmer, J. J. Structural determinants of RhoA binding and nucleotide exchange in leukemia-associated Rho guanine-nucleotide exchange factor. *J. Biol. Chem.* **279**, 47352–47362 (2004).
49. Kristelly, R., Earnest, B. T., Krishnamoorthy, L. & Tesmer, J. J. Preliminary structure analysis of the DH/PH domains of leukemia-associated RhoGEF. *Acta Crystallogr. D. Biol. Crystallogr.* **59**, 1859–1862 (2003).
50. Wienken, C. J., Baaske, P., Rothbauer, U., Braun, D. & Duhr, S. Protein-binding assays in biological liquids using microscale thermophoresis. *Nat. Commun.* **1**, 100 (2010).
51. Battye, T. G., Kontogiannis, L., Johnson, O., Powell, H. R. & Leslie, A. G. iMOSFLM: a new graphical interface for diffraction-image processing with MOSFLM. *Acta Crystallogr. D. Biol. Crystallogr.* **67**, 271–281 (2011).
52. Evans, P. R. An introduction to data reduction: space-group determination, scaling and intensity statistics. *Acta Crystallogr. D. Biol. Crystallogr.* **67**, 282–292 (2011).
53. McCoy, A. J. et al. Phaser crystallographic software. *J. Appl Crystallogr.* **40**, 658–674 (2007).
54. Wei, Y. et al. Crystal structure of RhoA-GDP and its functional implications. *Nat. Struct. Biol.* **4**, 699–703 (1997).
55. Liebschner, D. et al. Macromolecular structure determination using X-rays, neutrons and electrons: recent developments in Phenix. *Acta Crystallogr. D. Struct. Biol.* **75**, 861–877 (2019).
56. Emsley, P. & Cowtan, K. Coot: model-building tools for molecular graphics. *Acta Crystallogr. D. Biol. Crystallogr.* **60**, 2126–2132 (2004).
57. Lin, Y., Watanabe-Chailland, M. & Zheng, Y. Protocol for structural and biochemical analyses of RhoA GTPase. *STAR Protoc.* **2**, 100541 (2021).
58. Williamson, M. P. Using chemical shift perturbation to characterise ligand binding. *Prog. Nucl. Magn. Reson. Spectrosc.* **73**, 1–16 (2013).
59. Lee, W., Tonelli, M. & Markley, J. L. NMRFAM-SPARKY: enhanced software for biomolecular NMR spectroscopy. *Bioinformatics* **31**, 1325–1327 (2015).
60. Haspel, N., Jang, H. & Nussinov, R. Active and Inactive Cdc42 Differ in Their Insert Region Conformational Dynamics. *Biophys. J.* **120**, 306–318 (2021).
61. Liao, T. J., Jang, H., Fushman, D. & Nussinov, R. Allosteric KRas4B Can Modulate SOS1 Fast and Slow Ras Activation Cycles. *Biophys. J.* **115**, 629–641 (2018).
62. Senyuz, S., Jang, H., Nussinov, R., Keskin, O. & Gursoy, A. Mechanistic Differences of Activation of Rac1(P29S) and Rac1(A159V). *J. Phys. Chem. B* **125**, 3790–3802 (2021).
63. Brooks, B. R. et al. CHARMM: the biomolecular simulation program. *J. Comput. Chem.* **30**, 1545–1614 (2009).
64. Huang, J. et al. CHARMM36m: an improved force field for folded and intrinsically disordered proteins. *Nat. Methods* **14**, 71–73 (2017).
65. Klauda, J. B. et al. Update of the CHARMM all-atom additive force field for lipids: validation on six lipid types. *J. Phys. Chem. B* **114**, 7830–7843 (2010).
66. Phillips, J. C. et al. Scalable molecular dynamics on CPU and GPU architectures with NAMD. *J. Chem. Phys.* **153**, 044130 (2020).
67. Humphrey, W., Dalke, A. & Schulten, K. VMD: visual molecular dynamics. *J. Mol. Graph.* **14**, 33–38 (1996). 27-38.
68. Pettersen, E. F. et al. UCSF Chimera-a visualization system for exploratory research and analysis. *J. Comput. Chem.* **25**, 1605–1612 (2004).

Acknowledgements

This study was funded by NIH grants R01 HL147536 (Y.Z.), U54 DK126108 (Y.Z.), P01 HL158688 (Y.Z.), and CancerFree KIDS Foundation (CFK 400488, Y.L.). This research used resources from the Advanced Photon Source at the Argonne National Laboratory. The Lilly Research Laboratories Collaborative Access Team (LRL-CAT) beamline at Sector 31 of the Advanced Photon Source was provided by Eli Lilly Company, which operates the facility. All simulations were performed using the high-performance computational facilities of the Biowulf PC/Linux cluster at the National Institutes of Health (NIH), Bethesda, MD, USA (https://hpc.nih.gov/). This project has been funded in whole or in part with federal

funds from the National Cancer Institute (NCI), NIH, under contract HHSN261201500003I. The content of this publication does not necessarily reflect the views or policies of the Department of Health and Human Services, nor does the mention of trade names, commercial products, or organizations imply endorsement by the US Government. This Research was supported (in part) by the Intramural Research Program of NIH, NCI, Center for Cancer Research. We thank Dr. Miki Watanabe at the CCHMC NMR-based Metabolomics Core for ^{31}P, ^{1}H-^{15}N HSQC, and NOESY NMR data collection and processing and Dr. Nicholas Nassar, who provided insight and suggestions for the research and comments that greatly improved the manuscript.

Author contributions

Y.L. designed, performed, and analyzed all experiments including crystallographic data acquisition and structure determination, and wrote the paper. T.A.R. assigned, analyzed and interpreted the 2D ^{1}H-^{15}N HSQC and 3D NOESY NMR data. S.S. designed, performed, analyzed the MD simulations, and wrote the paper. A.G., H.J., R.N. and O.K. supervised, designed, and analyzed the MD simulations. All authors reviewed, revised, and approved the final version of the article. Y.Z. designed, supervised, provided funding for all experiments, and wrote the paper. R.N. provided funding for the MD simulations.

Competing interests

The authors declare no competing interests.

Additional information

Supplementary information The online version contains supplementary material available at https://doi.org/10.1038/s41467-024-51445-z.

Correspondence and requests for materials should be addressed to Yuan Lin or Yi Zheng.

Peer review information *Nature Communications* thanks the anonymous reviewers for their contribution to the peer review of this work. A peer review file is available.

Reprints and permissions information is available at http://www.nature.com/reprints

Publisher's note Springer Nature remains neutral with regard to jurisdictional claims in published maps and institutional affiliations.

Open Access This article is licensed under a Creative Commons Attribution-NonCommercial-NoDerivatives 4.0 International License, which permits any non-commercial use, sharing, distribution and reproduction in any medium or format, as long as you give appropriate credit to the original author(s) and the source, provide a link to the Creative Commons licence, and indicate if you modified the licensed material. You do not have permission under this licence to share adapted material derived from this article or parts of it. The images or other third party material in this article are included in the article's Creative Commons licence, unless indicated otherwise in a credit line to the material. If material is not included in the article's Creative Commons licence and your intended use is not permitted by statutory regulation or exceeds the permitted use, you will need to obtain permission directly from the copyright holder. To view a copy of this licence, visit http://creativecommons.org/licenses/by-nc-nd/4.0/.

© The Author(s) 2024